Surface & Coatings Technology 258 (2014) 1039–1047

Contents lists available at ScienceDirect

Surface & Coatings Technology

journal homepage: www.elsevier.com/locate/surfcoat

Thickness-dependent fracture characteristics of ceramic coatings bonded on the alloy substrates

X.N. Li, L.H. Liang *, J.J. Xie, L. Chen, Y.G. Wei

LNM, Institute of Mechanics, Chinese Academy of Sciences, Beijing 100190, China

ARTICLE INFO

Article history:
Received 20 November 2013
Accepted in revised form 8 July 2014
Available online 16 July 2014

Keywords:
Thickness of coatings
Fracture modes
Three-point bending
Interface cohesive model

ABSTRACT

The ceramic coatings with different thicknesses in the range of 150 μm to 490 μm, bonded on the same alloy substrates, were obtained by the air plasma spray method. The crack evolution and the fracture characteristics of the samples were observed synchronously under the three-point bending load using a scanning electron microscope. The results show different fracture modes for the thinner and the thicker coating samples; the multiple transverse cracks, vertical to the interface between the coatings and the substrates, in the coatings are the main fracture mode for the samples with coatings thinner than about 200 μm, while the interface crack is the main fracture mode for the samples with coatings thicker than about 300 μm. Different fracture modes were theoretically analyzed based on the nonlinear delamination model, and the calculated critical thickness is 255 μm, which agrees well with the experimental result. The finite element simulations for the corresponding coatings with a series of thicknesses were carried out by introducing the interface cohesive model, and the simulations show results similar to those of the experimental observations. The study indicates that the fracture modes depend on the thickness of the coatings, and the critical thickness depends on the intrinsic properties of coatings and the interfaces between the coatings and the substrates, such as the elastic modulus, the interface strength and the fracture energy.

1. Introduction

Ceramic coatings are widely used in thermal barrier engineering, anti-corrosion and oxidation-resistance applications. Fracture and failure of the ceramic coatings affect the performance and service lifetime of the related structures and devices. For example, the ceramic thermal barrier coatings are usually used to provide thermal insulation for interior metallic components of blades of gas turbine engines from hot gas stream [1,2]. Once the ceramic coatings flaked off and the interfaces between the coatings and the metallic substrates fractured, the substrates exposed in high temperature environment would fail. The fracture characteristics of the coating systems have been studied by the uni-axial tension tests [3–6], and the interface fracture toughness was analyzed based on the Suo–Hutchinson model [7]. For example, Zhou et al. studied different fracture modes of the functionally grade material coatings and the non-functionally grade material coatings [3]. Qian et al. studied the crack initiation and the damage evolution in the sandwiched thermal barrier coating specimens [4]. Chen et al. studied the temperature effect on the fracture behavior of the thermal barrier coatings [5], etc. However, the thickness effect on the fracture modes of thermal barrier coatings is rarely reported. Although the thickness effect on the mechanical properties of the metallic alloy coatings was studied, which indicates that the effect is not obvious [8], the thickness effect on the ceramic coatings is unknown.

In this paper, two kinds of fracture modes of the ceramic coatings with different thicknesses, bonded on the same metallic substrates, are reported based on the in-situ three-point bending experiment, the theoretical analysis and the finite element simulations. The thickness dependence of the fracture modes provides a guide to optimize the design of coatings in the related devices serviced in mechanical and thermal conditions.

2. Experimental procedure

2.1. Specimen preparation

The thermal barrier coating samples used in this study consist of the YSZ (8 wt.% Y_2O_3 stabilized ZrO_2) top coatings prepared by the standard atmospheric plasma spraying method [9,10], the NiCrAlY (25.42 wt.% Cr–5.1 wt.% Al–0.48 wt.% Y) bond coatings prepared by the high velocity oxygen fuel method, and the Ni-based superalloy substrates [10]. The detailed preparation process and the microstructure of the coatings can be referred to Ref. [10]. There are two kinds of samples with coatings of different thicknesses, one kind with the thicker coatings of 350–490 μm thickness and the other kind with the thinner coatings of 150–200 μm; the detailed thickness of the coatings for ten representative samples can be seen in Table 1 (h_c), the thickness h_c actually

* Corresponding author.
E-mail address: lianglh@lnm.imech.ac.cn (L.H. Liang).

http://dx.doi.org/10.1016/j.surfcoat.2014.07.031
0257-8972/

Table 1
The thickness of the coatings h_c, the thickness of the substrates h_s, the width b of the representative samples, the load P at the transformation points of the load–displacement curves, the normal stress σ_i and the shear stress τ_i of the coatings at the interface.

Samples		h_c (μm)	h_s (mm)	b (mm)	P (N)	σ_i (MPa)	τ_i (MPa)
Thinner coatings	S1	166	1.334	3.14	383	360.4	15.4
	S2	151	1.349	3.04	431	397.6	18.5
	S3	186	1.314	3.14	355	399.3	15.3
	S4	199	1.301	3.24	407	392.6	14.8
	S5	169	1.331	3.26	405	459.3	15.5
Thicker coatings	S6	487	0.953	2.55	215	227.6	22.8
	S7	459	1.161	3	376	330.8	35.4
	S8	355	1.065	2.84	320	324.1	39.4
	S9	381	1.159	2.92	380	346.3	58.6
	S10	402	1.018	2.76	283	202.5	28.1

includes the thickness of the ceramic top coatings and the thickness of the bond coatings of about several decade microns to a hundred microns. The samples were fabricated to be the appropriate size with the length, the width and the thickness being about 15 mm, 3 mm and 1.5 mm, respectively.

2.2. In-situ three-point bending test

The samples were ground and polished, and then were placed in the sample room of the FEI Sirion 400 NC scanning electron microscope (SEM) for in-situ observation of the crack initiation and propagation under the load using the mechanical testing apparatus — Gatan Microtest 2000. The three-point bending measurements were carried out by the slight movement of the jig controlled by the mechanical testing apparatus, as shown in Fig. 1(a). The load was applied on the alloy substrate face, and two fulcrums contact the ceramic coating face as shown in Fig. 1(a) and (b), the span is 10 mm. The loading rate is 0.1 mm/min. The evolution of cracks in the side face with increasing load was observed and recorded by use of the SEM.

3. Experimental results

Fig. 2 shows the load–displacement curve of the thinner coating sample with the coating of 186 μm thickness and the corresponding crack evolution maps with increasing load under the three-point bending. It can be seen that the load increases with enhancing displacement firstly, when the load reaches the maximum value, an approximate plateau appears in the load–displacement curve, finally the load drops with enhancing displacement as shown in Fig. 2(a). The maximum load corresponds to the emergence of the multiple transverse cracks in the coating, vertical to the interface between the coating and the substrate, as shown in Fig. 2(b) (see maps III and IV, map III only shows a part of map IV due to the smaller field of vision), indicating that the normal stress in the coating reaches the tension strength of the coating, the detailed stress analysis will be given in Section 4.2, at the same time, the number of the transverse cracks saturates. After the maximum load, the transverse cracks in the coating become wider and propagate into the substrate further (map V in Fig. 2(b)), the metallic alloy substrate withstands the load mainly corresponding to the plateau in the load–displacement curve, and the obvious plastic sliding bands can be found in the substrate (maps IV and V in Fig. 2(b)). Note that the maps with different scale bars were taken for a clearer view. Also note that there are some tiny jumps in the load–displacement curve, corresponding to the points of stopping loading and taking pictures, where the load drops slightly without the change of the displacement, and after taking a picture each time, the load was resumed and applied continuously again.

Fig. 3 shows the load–displacement curve of the thicker coating sample with the coating of 459 μm thickness and the corresponding crack evolution maps with increasing load. The load–displacement

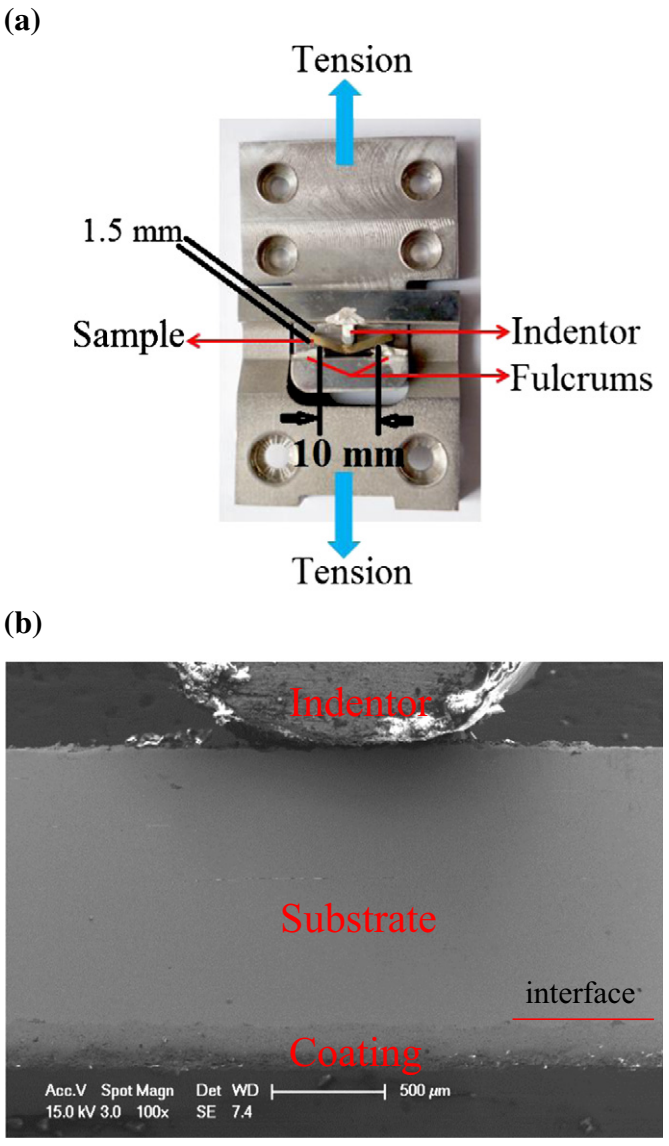

Fig. 1. The schematic illustration of the three-point bending test. (a) The jig for the sample under bending in the SEM. (b) The sample under the initial load, the side face view.

curve showed in Fig. 3(a) is similar to that of the thinner coating sample. Differently, the maximum load for the thicker coating sample corresponds to an obvious interface crack between the coating and the substrate, as shown in Fig. 3(b) (see maps III and IV, map III only shows a part of map IV), besides a larger transverse crack. It is resulted from that the shear failure dominates for the thicker coating systems and the interface energy release rate reaches the delamination energy, which will be discussed in detail in Section 4.1. Moreover, there is no obvious plastic sliding band in the substrate.

Fig. 4 shows the comparison of the load–displacement curves of the respective three samples with the thinner ($h_c < 170$ μm) and the thicker ($h_c > 350$ μm) coatings. It can be seen that the maximum loads for the thinner coating samples are usually higher than those for the thicker coating ones, which may imply that the thinner coating samples have better bending-resistance. After the peak loads, the loads drop faster for the thicker coating samples than for the thinner coating ones and there is no obvious plateau in the load–displacement curves of the thicker coating samples, because the interface crack between the coatings and the substrates occurs for the thicker coating samples concomitant with the larger elastic energy release and the plasticity dissipation contribution from the substrates is lower relatively. On the other hand,

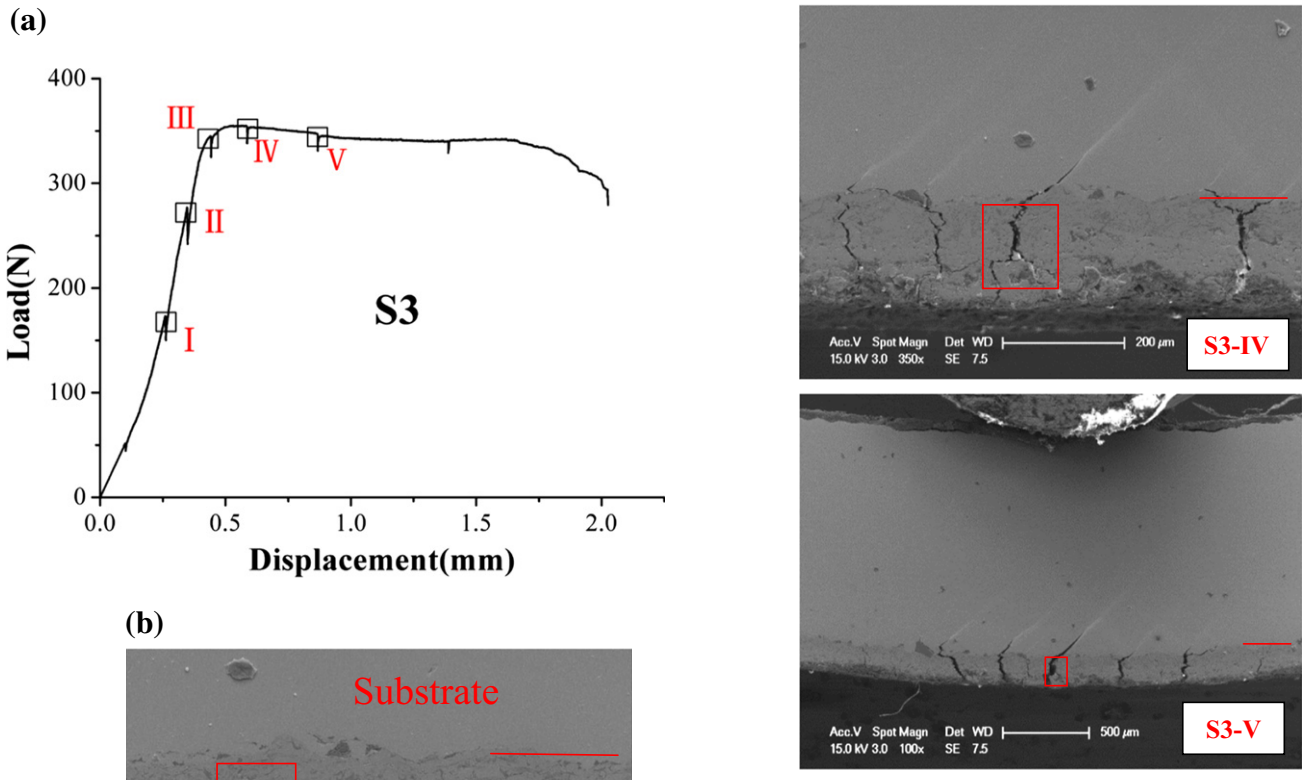

Fig. 2. The load–displacement curve (a) of the thinner coating sample S3 and the corresponding crack evolution maps I–V (b) obtained by the three-point bending in the SEM. The scale bars of I–V in (b) are 100, 100, 100, 200, and 500 μm, respectively. The squares in the maps denote the same location of the sample.

for the thinner coating systems with larger thickness of the metallic substrates, the plastic straining in the ductile substrates can lead to significant reduction in the interface crack driving force by dissipating energy as discussed in Ref. [11]. Recent tests of this type have succeeded without plasticity by bonding a stiff layer to the coating which enables much larger elastic energy release [12].

Fig. 5 shows the fracture maps of the representative sample with the thinner coating, corresponding to the failure point denoted in Fig. 4 (S1), from the side face view (Fig. 5(a)) and the bottom surface view (i.e. the surface of the coatings) (Fig. 5(b)). It can be seen that the multiple transverse cracks in the coating are the main fracture mode for the thinner coating sample, and the cracks propagate into the substrate at the larger deformation. The local interface crack, between the ceramic coating and the bond coating, occurs between two neighbor transverse cracks, and the local spallation of the ceramic coating occurs as shown in Fig. 5(a). Fig. 6 shows the fracture maps of the representative sample with the thicker coating, corresponding to the failure point denoted in Fig. 4 (S6), from the side face view (Fig. 6(a)) and the bottom surface view (Fig. 6(b)). It can be seen that the interface crack between the coating and the substrate (in detail between the bond coating and the substrate) is the main fracture mode for the thicker coating sample, and a larger transverse crack in the coating occurs, which is obvious as shown in the bottom surface map (Fig. 6b) and can be explained by the energy and stress analysis in Section 4. Although Figs. 5 and 6 only show the fracture maps of respective one sample for the thinner and the thicker coating samples, they are representative, other samples show the same fracture characteristics.

By comparing Fig. 5 with Fig. 6, different fracture modes of the samples with the thicker and the thinner coatings can be found. The fracture mode of the multiple transverse cracks makes the thinner coating samples present the better bending-resistance than the thicker coating samples with the fracture mode of the interface crack, as shown in Fig. 4, which agrees with the latest report on the fracture properties of the

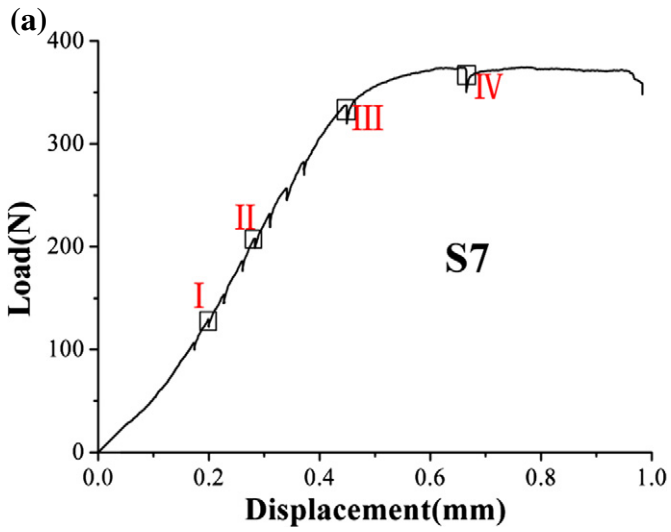

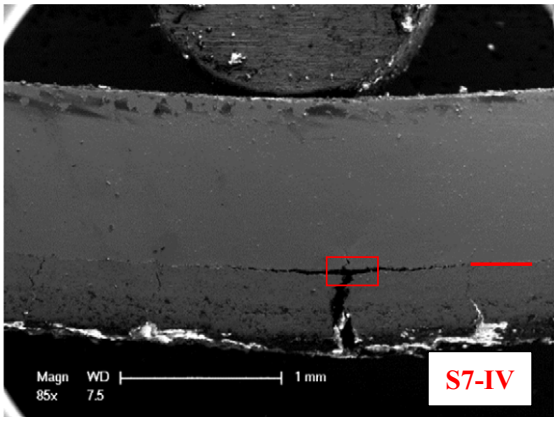

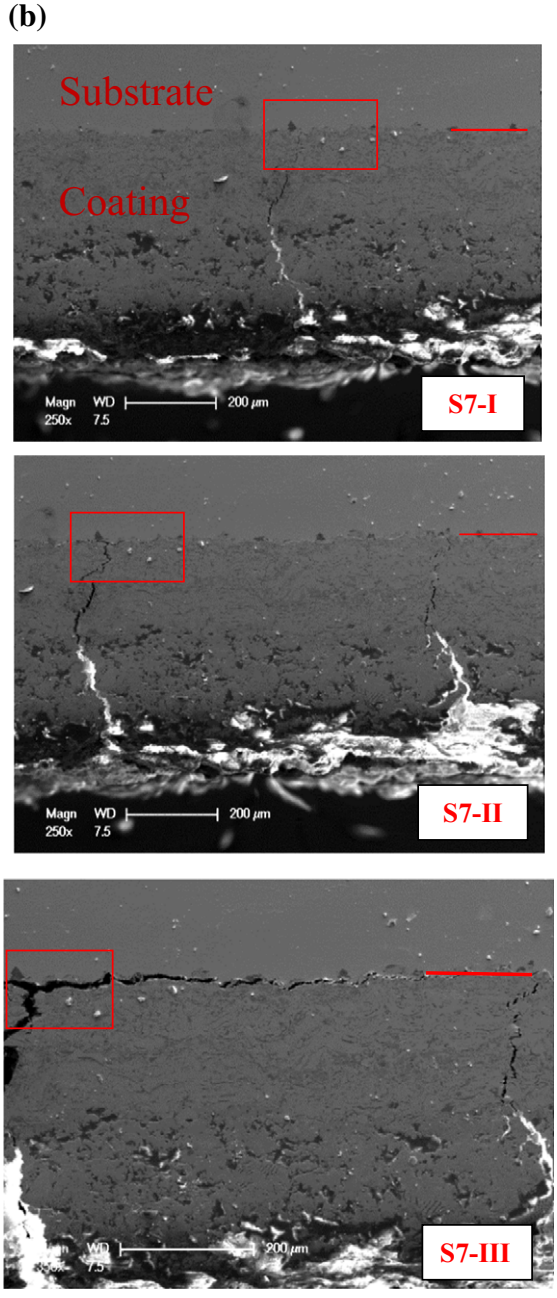

Fig. 3. The load–displacement curve (a) of the thicker coating sample S7 and the corresponding crack evolution maps I–IV (b). The scale bars of I–IV in (b) are 200 μm, 200 μm, 200 μm, and 1 mm, respectively. The squares in the maps denote the same location of the sample.

thermal barrier coatings [13] (referring to Figs. 4(c), 5(c) and 6 in Ref. [13]). In order to explain the experimental results and understand the thickness effect, theoretical analysis was carried out as follows.

4. Theoretical analysis

4.1. Interface crack

According to the nonlinear delamination model of thin films [14], a thin isotropic film of thickness h bonded to a thick substrate is subject to a uniform, equi-biaxial residual stress σ_R (referring to Fig. 1 in Ref. [14]). The elastic energy per unit area in the bonded film is $(1-\nu)h\sigma_R^2/E$, where E and ν are the Young's modulus and Poisson's ratio of the film, respectively. When delamination occurs as a long interface crack releasing the elastic energy without plastic deformation in the film, the energy release rate per unit of crack advance is

$$G = \frac{\left(1-\nu^2\right)h\sigma_R^2}{2E}. \tag{1}$$

The elastic films denote the coatings here. When the residual stress σ_R at the interface between the coatings and the substrates reaches the interface strength σ_b, the interface crack occurs, and the corresponding critical thickness h_{cr} is expressed as

$$h_{cr} = \frac{2EG_C}{(1-\nu^2)\sigma_b^2} \tag{2}$$

based on Eq. (1), where $G_C = 150\ \mathrm{J/m^2}$ was taken as the critical interface fracture energy between the coatings (bond coatings based on the experiments) and the substrates [15]. In Eq. (2), $E = 100$ GPa and $\nu = 0.2$ were taken for the coatings [16,17]. The interface strength σ_b between the coatings and the substrates is approximately 350 MPa as the strength of the mixed mode in the tension and the shear directions ($T_N = 350$ MPa and $T_S = 20$ MPa [17,18] are the tension and the shear strength, respectively). By substituting G_C and σ_b into Eq. (2), $h_{cr} = 255$ μm can be obtained. The result indicates that when the thickness of the coatings is larger than 255 μm, the interface crack occurs, which is in well agreement with the experimental observation shown in Figs. 3 and 6. The multiple transverse cracks in the coating occur for the coatings with thickness smaller than 255 μm, because the residual stress in the coatings reaches the strength of the coatings of 200 MPa ($T_N = T_S = 200$ MPa for the coatings based on the experiments and the related literatures [18,19]) as the following analysis.

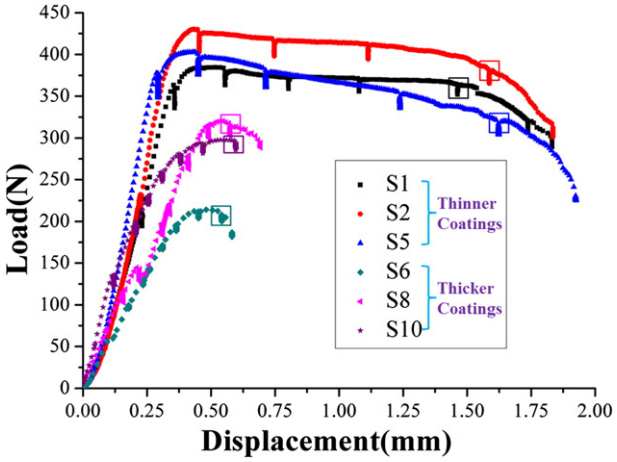

Fig. 4. The load–displacement curves of the representative three samples with the thinner (S1, S2 and S5) and the thicker coatings (S6, S8 and S10). The squares in the curves denote the failure points after the plateaus or the peak loads, and the corresponding fracture maps are given in Figs. 5 and 6, respectively for the thinner and the thicker coatings.

4.2. Transverse crack

The coating/substrate systems were treated simply as two-layer systems with the coatings and the substrates as shown in Fig. 7; h_c and h_s are the thicknesses of the coatings and the substrates, respectively, as shown in Table 1 (note their different units), and ς is the distance between the interface and the neutral layer of the systems. The location of the neutral line can be calculated as [8],

$$\varsigma = \frac{E_s h_s^2 - E_c h_c^2}{2(E_s h_s + E_c h_c)}, \tag{3}$$

where the elastic moduli of the coatings and the substrates E_c = 100 GPa and E_s = 200 GPa were taken [16,20], respectively. The normal stress σ_i and the shear stress τ_i at the interface for the coatings can be calculated by Eqs. (4) and (5) [21],

$$\sigma_i = \frac{P l E_c \varsigma}{4\langle EI\rangle}, \tag{4}$$

$$\tau_i = \frac{P E_c \left[(h_c+\varsigma)^2 - \varsigma^2\right]}{4\langle EI\rangle}, \tag{5}$$

where the load P was taken as the loads at the transformation points of the load–displacement curves corresponding to the interface crack for the thicker coating systems or the penetrating (through the interface) of the transverse crack for the thinner coating systems, l = 10 mm is the span length, $\langle EI\rangle = E_s I_s + E_c I_c$ is the equivalent bending stiffness, $I_s = \int_{\varsigma-h_s}^{\varsigma} by^2 dy$ and $I_c = \int_{\varsigma}^{\varsigma+h_c} by^2 dy$ are the moment of inertia of the substrates and the coatings, respectively, and b is the width of the specimens as shown in Table 1. The shear stress is consecutive at the interface, i.e., $(\tau_i)_s = (\tau_i)_c$, the subscripts s and c represent the substrates and the coatings, respectively. On the other hand, the normal stress is not consecutive at the interface, and $(\sigma_i)_c$ for the coatings was considered actually here, corresponding to the minimum residual normal stress of the coatings. The calculated normal stress and the shear stress at the coating/substrate interface are shown in Table 1. It can be seen that the normal stress σ_i and the shear stress τ_i at the interface for the thinner coating systems are 360.4–459.3 MPa and 14.8–18.5 MPa, respectively, and those for the thicker coating systems are 202.5–346.3 MPa and 22.8–58.6 MPa, respectively. Therefore, the tensile strength and the shear strength of the interface may be 346.3–360.4 MPa and 18.5–22.8 MPa, respectively, agreeing with the values as taken in Section 4.1 (T_N = 350 MPa and T_S = 20 MPa), and the shear strength is also close to some data in the literatures [17,18,22]. For the thinner coatings, the residual normal stress is obviously larger than the tension strength of the coatings of 200 MPa, thus the transverse cracks in the coatings emerge. And the shear stress is smaller than the shear strength of the interface of 20 MPa, thus there is no obvious interface crack in the thinner coating systems and the tension failure dominates. In order to validate the experimental results and the theoretical analysis, the finite element simulations for the samples with the coatings of a series of thicknesses, based on the interface cohesive model, were carried out as follows.

5. Finite element simulations

5.1. Three-point bending model

A 2D numerical model was built with the commercially available FEM code ABAQUS; the model includes two layers, the coating and the substrate as shown in Fig. 8(a). The length and the total thickness of the model are 10 mm and 1.5 mm, respectively, and a series of thicknesses of 50, 150, 300, 450 and 600 μm for the coatings were taken corresponding to the thinner and the thicker coatings in the experiments. The boundary condition is also shown in Fig. 8(a), two ends of the upside of the substrate were simply supported, and the load was applied on the middle of the upside of the substrate.

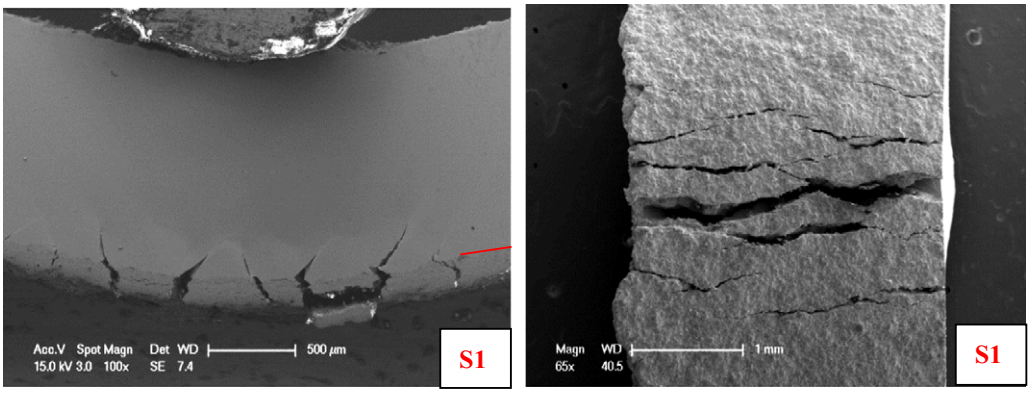

Fig. 5. The fracture maps corresponding to the failure point of the sample S1 with the thinner coating based on the three-point bending in the SEM. (a) The side face map (scale bar 500 μm) and (b) the bottom surface map of the coating (scale bar 1 mm).

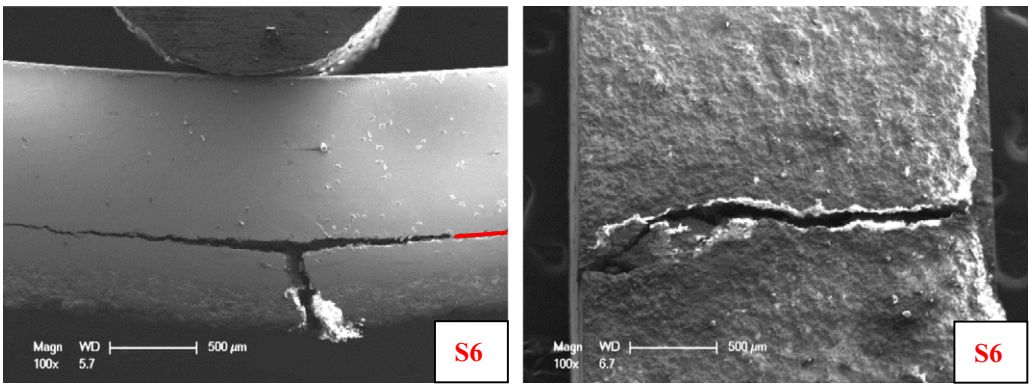

Fig. 6. The fracture maps corresponding to the failure point of the sample S6 with the thicker coating. (a) The side face map and (b) the bottom surface map. The scale bars are both 500 μm.

The coating and the substrate sheets were meshed using the four-node plane strain elements, the coating includes 100 segments, and the four-node interface cohesive elements were adopted between the neighbor segments of the coating and between the coating and the substrate as shown in Fig. 8(a). The linear elastic constitutive relation was considered for the coatings, and the elastoplastic constitutive model with linear hardening was considered for the substrates as shown in Eq. (6),

$$\sigma = \begin{cases} E_s\varepsilon, & \varepsilon \le \dfrac{\sigma_y}{E_s} \\ \sigma_y + E_s^*\left(\varepsilon - \dfrac{\sigma_y}{E_s}\right), & \varepsilon > \dfrac{\sigma_y}{E_s} \end{cases}, \tag{6}$$

where σ and ε are the stress and the strain of the substrates, respectively, σ_y is the yield strength of the substrates and was taken as 850 MPa based on our experiment and the literature [23], E_s^* is the hardening modulus and was taken as 1/10 of the elastic modulus of the substrates based on our experiment. The elastic modulus E and the Poisson's ratio ν are respectively $E_c = 100$ GPa, $\nu_c = 0.2$ for the coatings [16,17], and $E_s = 200$ GPa, $\nu_s = 0.3$ for the substrates [16,20].

5.2. Interface cohesive model

Cohesive zone models (CZMs) based on the traction laws are well suitable to describe the interface decohesion. The CZMs require traction–separation (T–S) relations for characterizing their constitutive laws. It has been established that the peak value and area of the T–S curve are vital for capturing the interface separation behavior [24]. The bilinear T–S relation was adopted here as simplicity for the interface elements between the coating neighbor segments and between the coating and the substrate as shown in Fig. 8(b). Fig. 8(b) represents the cohesive relation in the mixed mode of the tension and the shear, i.e., the total traction–separation response. For the pure tension and the pure shear modes, similar cohesive relations were assumed and expressed as

$$\sigma = \begin{cases} T_N\dfrac{\delta_N}{\delta_N^0}, & \delta_N \le \delta_N^0 \\ T_N\dfrac{\delta_N^f - \delta_N}{\delta_N^f - \delta_N^0}, & \delta_N \ge \delta_N^0 \end{cases} \quad \text{(normal direction)} \tag{7}$$

$$\tau = \begin{cases} T_S\dfrac{\delta_S}{\delta_S^0}, & \delta_S \le \delta_S^0 \\ T_S\dfrac{\delta_S^f - \delta_S}{\delta_S^f - \delta_S^0}, & \delta_S \ge \delta_S^0 \end{cases} \quad \text{(tangent direction)}$$

when the normal separating displacement $\delta_N > 0$, where σ and τ represent the normal and the tangent separating stress, respectively, δ and T represent the displacement and the maximum separating stress (i.e. the strength), respectively, the subscripts N and S represent the normal and the tangent directions, respectively, the superscripts 0 and f represent the critical displacement corresponding to the strength T (the damage initiation) and the fracture displacement corresponding to the complete failure, respectively. When $\delta_N < 0$, only the tangent stress is effective. The critical fracture energy G_C in the normal and the tangent directions is respectively

$$G_{NC} = \int_0^{\delta_N^f} \sigma \mathrm{d}\delta_N = \frac{1}{2}T_N\delta_N^f$$
$$G_{SC} = \int_0^{\delta_S^f} \tau \mathrm{d}\delta_S = \frac{1}{2}T_S\delta_S^f. \tag{8}$$

As the load increases beyond a critical value, the interface begins to soften and degrade, namely, the interface is in the damaged (or softening) state. Typically, the damage initiates when a certain criterion is satisfied. For the mixed mode showed in Fig. 8(b), the maximum stress criterion was adopted to characterize the interfacial damage, which is described as [25]

$$\mathrm{MAX}\left\{\frac{\langle\sigma_N\rangle}{T_N}, \frac{\tau_S}{T_S}\right\} = 1, \tag{9}$$

where $\langle\rangle$ represents the Macaulay bracket defined by $\langle x\rangle = (|x| + x)/2$ with the usual interpretation that a pure compressive deformation or stress state does not initiate damage. It is assumed that interfacial damage occurs when Eq. (9) is satisfied and a single damage variable D based on the total displacement δ_m of the mixed mode was introduced $\left(\delta_m = \sqrt{\langle\delta_N\rangle^2 + \delta_S^2}\right)$ [26,27] as

$$D = \begin{cases} 0, & \delta_m \le \delta_m^0 \\ \dfrac{\delta_m^f\left(\delta_m - \delta_m^0\right)}{\delta_m\left(\delta_m^f - \delta_m^0\right)}, & \delta_m^0 < \delta_m < \delta_m^f \\ 1, & \delta_m \ge \delta_m^f \end{cases}. \tag{10}$$

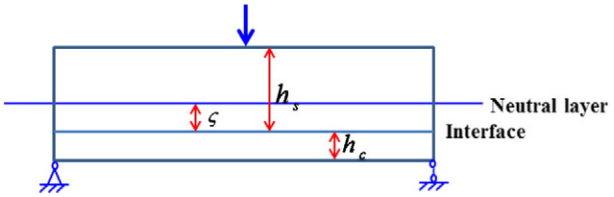

Fig. 7. The simplified model of two-layer systems in the three-point bending test.

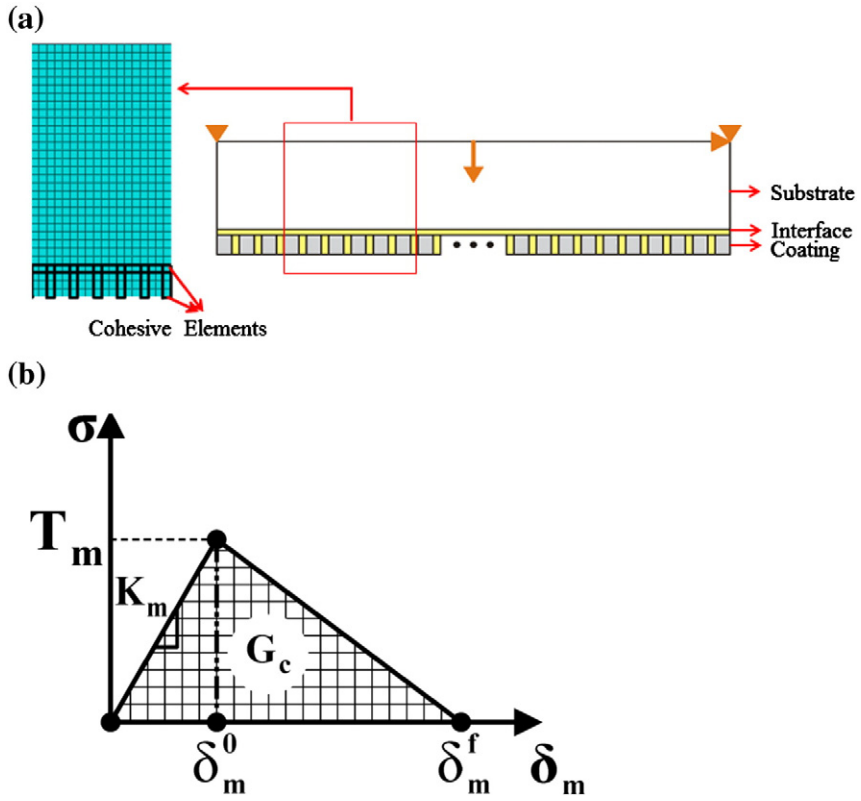

Fig. 8. The finite element model. (a) The schematic illustration of the coating/substrate systems under the three-point bending. (b) The bilinear interface cohesive (T–S) model in the mixed mode with the subscript *m* representing the mixed mode.

The interface fracture energy can be termed as the mixed mode fracture energy, and the power exponential criterion [28] was employed to describe the mixed mode fracture,

$$\left(\frac{G_N}{G_{NC}}\right)^{\alpha}+\left(\frac{G_S}{G_{SC}}\right)^{\alpha}=1, \tag{11}$$

where G_N and G_S represent the work done by the traction in the normal and the shear directions, respectively, G_{NC} and G_{SC} are the required critical energy for the interface fracture defined by Eq. (8), and the power exponential α was taken as 1. The total critical fracture energy can be determined by $G_C = G_N + G_S$ when Eq. (11) is satisfied. Note that the bilinear CZM constitutive equation used here (Eq. (7)) is not directly coupled, not like the quadratic function and the coupled separation laws [29,30]. Considering that the predictions based on the CZM appear to be insensitive to the details of the traction–separation law generally, being dependent on two characteristic parameters, i.e., the strength and the toughness [31], the simple bilinear separation laws were used here, the tension and shear directions were coupled through the mixed-mode failure criterion Eq. (11) as did in Ref. [31].

For the cohesive elements between the coating segments, $T_N = T_S =$ 200 MPa was assumed and $G_{NC} = G_{SC} = 20$ J/m^2 [18,19] was adopted. For the cohesive elements between the coatings and the substrates, $T_N = 350$ MPa and $T_S = 20$ MPa were taken referring to the experimental results [17,18], and $G_{NC} = G_{SC} = 150$ J/m^2 [15] was adopted referring to the related literature about the thermal barrier coatings. The stiffness K in the interface cohesive model showed in Fig. 8(b) is the slope of the initial segment of the traction–separation (T–S) curve and was taken to satisfy the relation of $\delta^f/\delta^0 = 4$ considering that the value of δ^f is several times that of δ^0 generally. Note that the cohesive zone model exhibits a softening behavior, which often results in serious convergence issues in finite element simulations. Thus, to enhance computation convergence, viscous regularization options in ABAQUS were used for the cohesive elements. The effect of the viscosity coefficient on result accuracy was also investigated by taking several different viscosity values of 0.001, 0.0005, 0.0003, 0.0002, 0.0001, and 0.000025. When the viscosity is larger (0.001), the error is larger. When the viscosity is 0.0002, the crack map and the crack number are almost the same as those based on the simulation with the viscosity of 0.0001. When the viscosity is smaller (0.000025), the simulation is not converged. Finally, 0.0001 was used as was in the previous experience [32] considering the economic convergence time, and which is also close to the stable result as discussed in the literature [33].

6. Simulation results

Fig. 9(a)–(e) shows the fracture characteristics based on the simulation results for the bending models with the coatings of 50, 150, 300, 450 and 600 μm thicknesses, respectively; the results show rough agreement with the experiment. For the thinner coatings with thicknesses of 50, 150 and 300 μm, the multiple transverse cracks in the coating are the main fracture mode, and for the thicker coatings of 450 and 600 μm, the interface crack is the main fracture mode. Note that the transverse cracks propagate through the interface into the substrates for the thinner coating systems in the experiments, while this phenomenon is not observed in the simulations, which is resulted from that the interface elements were not adopted for the substrates in the simulations and thus the substrates do not crack even at the larger load, and accordingly, the local interface crack occurs. For the thicker coating systems, the obvious interface crack releases the stored elastic energy in the deformation that reaches the critical delamination energy as discussed in Section 4.1.

Note that the critical fracture energies (toughnesses) in the interface cohesive model were taken referring to the related literatures, and the

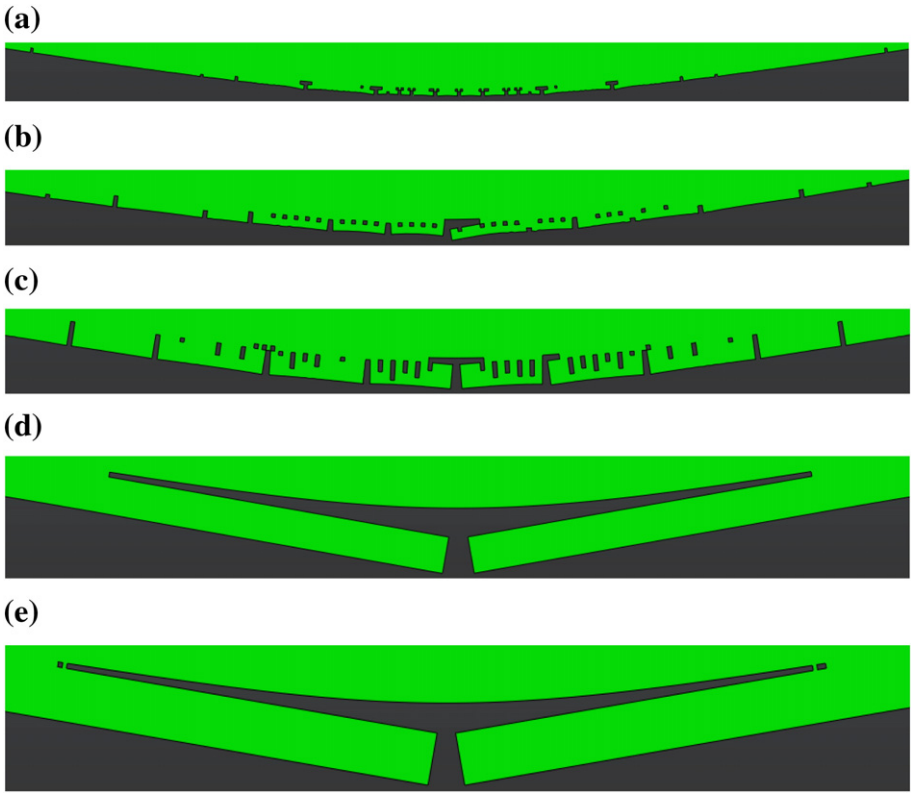

Fig. 9. The fracture modes of the coating/substrate systems with the coating of (a) 50, (b) 150, (c) 300, (d) 450, and (e) 600 μm thicknesses, respectively, at the displacement of 1–15 mm based on the finite element simulations of the three-point bending.

normal and the shear directions were assumed to be same for simplicity. The sensitivity analysis of the parameters was also carried out. For example, when the different values of the toughness were taken, $G_{NC} = 20\ J/m^2$, $G_{SC} = 40\ J/m^2$ for the coatings and $G_{NC} = 75\ J/m^2$, $G_{SC} = 150\ J/m^2$ for the interface between the coatings and the substrates, i.e., the Mode II toughness is twice the Mode I toughness as usual, there is no obvious influence on the final simulation results.

7. Conclusions

In summary, the thickness-dependent fracture characteristics of ceramic coating/metallic substrate systems were found by the in-situ three-point bending experiment with a designed jig and the finite element simulations based on the interface cohesive model. When the thickness of the coatings is smaller than about 200 μm, the multiple transverse cracks occur in the coatings and propagate into the substrates with increasing deformation. When the thickness of the coatings is larger than about 300 μm, the interface crack between the coatings and the substrates is the main fracture mode. The nonlinear delamination model was used to explain the experimental results well, and the calculated critical thickness is 255 μm. Moreover, the simulation results for the coatings with a series of thicknesses are roughly in agreement with the experimental observations. When the residual stress in the coatings reaches the tension strength of the ceramic coatings with loading, the multiple transverse cracks occur in the thinner coatings due to the tension failure that dominates. And when the thickness of the coatings is larger than the critical thickness, the delamination between the coatings and the substrates occurs due to the shear failure that dominates. The critical thickness and the fracture characteristics are related to the intrinsic properties of the coatings and the interfaces between the coatings and the substrates, such as the elastic modulus, the interface strength, and the fracture energy.

Conflict of interest

None.

Acknowledgment

This work was supported by the National Basic Research Programs of China (No. 2012CB937500), the NSFC grants of China (Nos. 10802088, 11372318, 11023001, 11021262, 10932011 and 91216108), and the CAS/SAFEA International Partnership Program for Creative Research Teams.

References

[1] A.G. Evans, D.R. Mumm, J.W. Hutchinson, G.H. Meier, F.S. Pettit, Prog. Mater. Sci. 46 (2001) 505.
[2] N.P. Padture, M. Gell, E.H. Jordan, Science 296 (2002) 280.
[3] Y.C. Zhou, T. Tonomori, A. Yoshida, L. Liu, G. Bignall, T. Hashida, Surf. Coat. Technol. 157 (2002) 118.
[4] L.H. Qian, S.J. Zhu, Y. Kagawa, T. Kubo, Surf. Coat. Technol. 173 (2003) 178.
[5] Z.B. Chen, Z.G. Wang, S.J. Zhu, Surf. Coat. Technol. 205 (2011) 3931.
[6] W.G. Mao, C.Y. Dai, L. Yang, Y.C. Zhou, Int. J. Fract. 151 (2008) 107.
[7] Z. Suo, J.W. Hutchinson, Int. J. Fract. 43 (1990) 1.
[8] H. Deng, H. Shi, S. Tsuruoka, Surf. Coat. Technol. 204 (2010) 3927.
[9] Z. Chen, R.W. Trice, M. Besser, X. Yang, D. Sordelet, J. Mater. Sci. 39 (2004) 4171.
[10] L.H. Liang, H. Wei, X.N. Li, Y.G. Wei, Surf. Coat. Technol. 236 (2013) 525.
[11] M.R. Begley, H.N.G. Wadley, J. Am. Ceram. Soc. 94 (s1) (2011) s96.
[12] R.G. Hutchinson, J.W. Hutchinson, J. Am. Ceram. Soc. 94 (Suppl. s1) (2011) s85.
[13] L. Yang, Z.C. Zhong, J. You, Q.M. Zhang, Y.C. Zhou, W.Z. Tang, Surf. Coat. Technol. 232 (2013) 710.
[14] Y.G. Wei, J.W. Hutchinson, J. Mech. Phys. Solids 45 (1997) 1137.
[15] T.W. Clyne, S.C. Gill, J. Therm. Spray Technol. 5 (1996) 401.
[16] J.Y. Kwon, J.H. Lee, Y.G. Jung, U. Paik, Surf. Coat. Technol. 201 (2006) 3483.
[17] Z.H. Xu, Y. Yang, P. Huang, X. Li, Acta Mater. 58 (2010) 5972.
[18] P.F. Zhao, C.A. Sun, X.Y. Zhu, F.L. Shang, C.J. Li, Surf. Coat. Technol. 204 (2010) 4066.
[19] A. Rabiei, A.G. Evans, Acta Mater. 48 (2000) 3963.
[20] N. Zotov, M. Bartsch, G. Eggeler, Surf. Coat. Technol. 203 (2009) 2064.

[21] R. Beydon, G. Bernhart, Y. Segui, Surf. Coat. Technol. 126 (2000) 39.
[22] P.F. Zhao, F.L. Shang, J. Zhejiang Univ.-Sci. A 11 (2010) 794.
[23] L.Z. He, Q. Zheng, X.F. Sun, G.C. Hou, H.R. Guan, Z.Q. Hu, Mater. Sci. Eng. A 380 (2004) 340.
[24] L.B. Freund, S. Suresh, Thin Film Materials: Stress, Defect Formation and Surface Evolution, Cambridge University Press, Cambridge, 2003.
[25] W. Xu, Y.G. Wei, Comput. Mater. Sci. 53 (2012) 444.
[26] C. Balzani, W. Wagner, Eng. Fract. Mech. 75 (2008) 2597.
[27] M.F.S.F. de Moura, R.D.S.G. Campilho, J.P.M. Goncalves, J. Adhes. Sci. Technol. 23 (2009) 1477.
[28] Y. Mi, M.A. Crisfield, G.A.O. Davies, H.B. Hellweg, J. Compos. Mater. 32 (1998) 1246.
[29] J.L. Hogberg, Int. J. Fract. 141 (2006) 549.
[30] V. Tvergaard, J.W. Hutchinson, J. Mech. Phys. Solids 41 (1993) 1119.
[31] J.P. Parmigiani, M.D. Thouless, J. Mech. Phys. Solids 54 (2006) 266.
[32] L. Chen, Y.G. Wei, Int. J. Damage Mech. 23 (2014) 25.
[33] B. Li, Y.Z. Li, J. Su, Compos. Part B 58 (2014) 217.